Control Engineering Practice 165 (2025) 106585

Contents lists available at ScienceDirect

Control Engineering Practice

journal homepage: www.elsevier.com/locate/conengprac

Optimisation-based tuning of nonlinear controllers for targeted dynamics: Methodology and a demonstrative wind energy case

Demián García-Violini [a,b,c], Carolina A. Evangelista [b,d], Yerai Peña-Sanchez [c,e,*], Paul Puleston [b,d]

[a] Departamento de Ciencia y Tecnología, Universidad Nacional de Quilmes, Roque Saenz Peña 352, B1876, Bernal, Buenos Aires, Argentina
[b] Consejo Nacional de Investigaciones Científicas y Técnicas (CONICET), CABA, C1425 FQB, Argentina
[c] Centre for Ocean Energy Research, Maynooth University, Maynooth W23 F2H6, Co. Kildare, Ireland
[d] Instituto LEICI, Facultad de Ingeniería/UNLP-CONICET, La Plata, Buenos Aires, Argentina
[e] Fluid Mechanics Department, Mondragon University, Loramendi 4, 20500, Arrasate, Spain

ARTICLE INFO

Keywords:
Optimisation-based tuning
Nonlinear control
Wind energy systems
Closed-loop dynamics
Sliding mode control

ABSTRACT

Tuning controllers for nonlinear systems remains a significant challenge due to their inherent complexity and the lack of systematic design methodologies. This study presents a practical, versatile, and robust optimisation-based procedure for tuning nonlinear controllers, including linear ones, offering a structured alternative to the traditional trial-and-error tuning strategies commonly used in practice. A key contribution of the proposed methodology is the explicit definition and achievement of target closed-loop dynamic behaviours in nonlinear systems, which is analogous to classical dynamics in linear control. By leveraging global optimisation techniques, the procedure systematically identifies controller parameters that minimise deviations from predefined dynamic targets while ensuring robustness and stability across a range of operating conditions. The approach addresses the nonlinear response of the controlled system and provides an intuitive and customisable framework for shaping closed-loop dynamics according to design objectives. The methodology is validated through its application to a wind turbine control problem, demonstrating its ability to tune both proportional–integral (PI) and super-twisting sliding mode controllers (SMC) effectively. The results highlight the sensitivity of nonlinear controllers to parameter selection and underscore the benefits of a systematic tuning approach in achieving consistent performance, preventing actuator saturation, and ensuring system longevity. This study offers a powerful and generalisable solution for tuning controllers in complex nonlinear systems, enabling practitioners to move beyond empirical tuning practice.

1. Introduction

Nonlinear systems pose a fundamental challenge in control engineering due to their complex dynamics, sensitivity to environmental variations, and the presence of uncertainties. In many practical applications, traditional linear control methods often fail to deliver optimal performance. This underscores the need for nonlinear control strategies, which offer the flexibility required to robustly manage such complexities and enhance system stability and performance under dynamic conditions. However, a significant obstacle in implementing nonlinear controllers is the absence of general, systematic tuning methods that can be applied across a wide range of nonlinear systems (Slotine et al., 1991). Most existing tuning approaches are tailored to specific system structures and rely on analytical tractability, which limits their broader applicability. While well-established techniques, like those based on Jacobian linearisation (Goodwin et al., 2001), can work under certain conditions, they become inadequate when hard nonlinearities or the absence of smooth derivatives complicate the behaviour of the system (Hiskens, 2002; Slotine et al., 1991). In response, nonlinear control approaches provide a positive alternative, offering greater flexibility in addressing complex dynamics. However, the challenge persists: not only is there a lack of systematic tuning methodologies for nonlinear controllers, but the very nature of nonlinear systems also complicates tuning, even when using simpler linear control strategies. Additionally, nonlinear controllers can exhibit high sensitivity to control parameters, leading to significant changes in the time response even with minimal parameter variations. As a result, practitioners often resort to trial-and-error tuning methods, which, although sometimes yielding acceptable

* Corresponding author.
E-mail addresses: ddgv83@gmail.com (D. García-Violini), cae@ing.unlp.edu.ar (C.A. Evangelista), ypena@mondragon.edu (Y. Peña-Sanchez), puleston@ing.unlp.edu.ar (P. Puleston).

https://doi.org/10.1016/j.conengprac.2025.106585
Received 16 May 2025; Received in revised form 10 September 2025; Accepted 11 September 2025
Available online 20 September 2025

performance, remain time-consuming and suboptimal. These challenges highlight the critical need for more efficient, systematic tuning methodologies to fully harness the potential of nonlinear control. Within this context, global optimisation techniques can provide a robust approach to overcoming the challenges associated with tuning nonlinear control systems (Locatelli & Schoen, 2013). With increasing computational power, these methods offer a structured and efficient alternative to traditional trial-and-error calibration (Rosendo et al., 2021).

Two main categories of optimisation-based control tuning strategies can be identified: for (i) linear controllers, and (ii) nonlinear controllers. In the first category, metaheuristic algorithms have been explored to enhance control performance, as seen in Mpanza and Pedro (2021). Additionally, systematic optimisation-based methodologies have been applied in power systems, as demonstrated in Hiskens (2002), which employs trajectory sensitivities to optimise nonlinear power system stabilisers and improve post-disturbance stability. In the second category, global optimisation methods have been used for sliding mode control (SMC) tuning (Khalil, 1996; Utkin, 1992). Notably, (Rosendo et al., 2021) applies interval arithmetic-based global optimisation to ensure sliding mode existence under bounded uncertainties, focusing on tuning the sliding surface relative to a first-order SMC rather than the full control law. While this methodology provides robustness guarantees, it does not explicitly optimise for a predefined closed-loop dynamic. In contrast, as detailed in the following sections, the present study advances the global optimisation framework by optimising the entire control structure, with the added capability of integrating stability constraints into the optimisation process and explicitly enforcing a desired convergence behaviour. Furthermore, whereas (Rosendo et al., 2021) demonstrates its SMC tuning methodology on an unmanned underwater vehicle, the presented study evaluates the proposed optimisation-based tuning approach in a wind energy system, considering both a second-order SMC and a PI controller to demonstrate its applicability across different control paradigms. Overall, while the aforementioned methodologies demonstrate the potential of optimisation-based tuning in specific contexts (Hiskens, 2002; Mpanza & Pedro, 2021; Rosendo et al., 2021), they often lack the generality required for broader application across diverse control scenarios. Thus, the presented study aims to bridge that gap by introducing a unified, systematic approach applicable to various controller structures and performance specifications.

Recent contributions have further enriched this field by introducing heuristic and learning-based optimisation strategies tailored to nonlinear systems. For instance, particle swarm optimisation has been employed to tune nonlinear PID controllers with enhanced robustness and disturbance rejection in first order plus time delay (FOPTD) systems (Charkoutsis & Kara-Mohamed, 2023). Similarly, Pazmiño et al. (2024) investigated the application of advanced metaheuristics — such as ant colony and flower pollination algorithms — for tuning fractional PID controllers in nonlinear tank systems, demonstrating improved performance over classical techniques. Model-free approaches have also gained traction, notably through the use of reinforcement learning: (Bujgoi & Sendrescu, 2024) leverages twin-delayed deep deterministic (TD3) algorithms to optimise PID controllers in biotechnological processes, achieving superior tracking of nonlinear dynamics without requiring explicit system models. In another recent example, Zambrano-Gutierrez et al. (2024) introduced a hyper-heuristic-based method for tuning adaptive SMCs in Buck–Boost converters, effectively matching the optimisation strategy to the problem structure and achieving substantial improvements in transient performance. While these studies underscore the relevance and versatility of modern optimisation techniques, they typically focus on tuning specific controllers for particular applications and often optimise local performance metrics, such as overshoot or settling time, without explicitly shaping the desired closed-loop behaviour. In contrast, the methodology proposed in this work offers a general, system-independent framework that embeds convergence dynamics directly into the optimisation problem. This facilitates a principled and unified tuning process across diverse nonlinear systems and controller architectures, as illustrated in the presented wind turbine case study.

Inspired by the results in Peña-Sanchez et al. (2024), this study proposes a systematic and simple optimisation-based methodology for tuning nonlinear controllers, while also covering linear control structures, and is particularly well-suited for applications involving strongly nonlinear systems. A key feature of this approach is the explicit definition of target convergence closed-loop dynamic as a design specification, which is integrated into the optimisation process. Simultaneously, the entire control parametric structure is optimised to achieve the desired closed-loop convergence dynamics. The optimisation problem is formulated to enable controller tuning using global optimisation techniques, with pattern search chosen for implementation due to its proven effectiveness in this study, though other optimisation methodologies may also be applicable. Two control methodologies are considered: firstly, a super-twisting SMC, where stability constraints could be directly incorporated into the design algorithm; and secondly, a standard PI controller, which is widely used in industry and academia. While the proposed methodology is not restricted to these particular control structures, their selection is motivated by their complementary characteristics. The PI controller, as a special case within a broader family of nonlinear controllers, provides a well-established and systematically *tunable* approach that ensures steady-state convergence within defined error tolerances. On the other hand, the super-twisting SMC represents a robust nonlinear alternative, particularly suited for systems with significant modelling uncertainties, without requiring precise model knowledge, as in techniques like backstepping or feedback linearisation (Khalil, 1996; Slotine et al., 1991). Furthermore, the second-order sliding mode formulation effectively mitigates chattering effects, making it more suitable for practical implementation. For demonstration and validation purposes, a wind turbine system is considered as an illustrative application case. Thus, both control strategies are studied in the context of a wind turbine model to assess their performance in managing the highly nonlinear dynamics of energy systems. The optimally tuned controllers are subsequently tested under various conditions, including different convergence dynamics, specifically, exponential and ramp target closed-loop responses, both of which are widely recognised in control theory and industrial applications (Evangelista et al., 2013), to further validate their effectiveness. To further evaluate the obtained control structures, a realistic wind model, based on the Kaimal spectrum, is used to generate turbulent wind profiles (Kaimal & Finnigan, 1985). The results demonstrate that the optimisation method consistently achieves optimal tuning solutions, effectively, when applicable as discussed in Section 5, enforcing the desired convergence dynamics. Notably, while this closed-loop specification enhances control performance, it also reveals a fundamental limitation of each control approach in achieving the defined target responses.

This work is motivated by the lack of systematic procedures for tuning nonlinear controllers. Moreover, although nonlinear control theory often guarantees stability or robustness, it typically overlooks the influence of parameter selection on transient behaviour. As a result, different tunings (though theoretically admissible) can lead to significantly different closed-loop dynamics. The proposed methodology addresses this gap by enabling a systematic, optimisation-based tuning process that explicitly enforces desired convergence behaviours, thus bringing nonlinear controller design closer to the goal-oriented strategies traditionally associated with linear control. The main contributions of this work are:

- A simple, general optimisation-based tuning framework applicable to both nonlinear and linear controllers;
- the explicit specification and enforcement of desired closed-loop convergence dynamics (e.g., exponential or ramp behaviour) as part of the tuning objective;

- a demonstration that even within the theoretical bounds of robust/stable nonlinear controllers, significantly different dynamic behaviours may emerge depending on parameter tuning, an issue directly addressed and exploited by the proposed methodology;
- integration of stability conditions into the optimisation formulation to ensure safe and robust control action; and
- validation through the application to a wind energy system using both a super-twisting sliding mode controller and a PI controller, illustrating the flexibility and practical relevance of the proposed approach across distinct control paradigms.

It is worth noting that, while the results include both PI and SM controllers applied to three test scenarios, this is not a comparative study. The inclusion of both controllers aims to illustrate the versatility and applicability of the proposed tuning methodology to systems with different levels of nonlinearity. Although both controllers are applied across the same scenarios, this is not intended as a comparative study. Rather, it aims to illustrate the broad applicability of the proposed tuning approach. Aspects such as comparative robustness, control effort, or computational complexity of PI versus SM controllers are not addressed in this study, since they fall outside its scope. Readers interested in such comparisons are referred to existing studies in the literature (e.g., Bendjeddou et al., 2021; Dekali et al., 2021; Haiqing et al., 1996; Papageorgiou, 2022; Papageorgiou & Edwards, 2021; Petronijević et al., 2017; Rubio et al., 2016; Sehab et al., 2023).

The remainder of this paper is organised as follows. Section 2 provides the analytical formulation of the proposed methodology, detailing the optimisation framework and its integration into the controller tuning process. Section 3 describes the considered control structures, including the super-twisting sliding mode controller and the PI controller used for comparison. Section 4 presents the application case of wind turbine control, outlining the tuning process and evaluating the controllers under different scenarios. Section 5 discusses the implications of the findings, including the benefits and limitations of enforcing an explicit closed-loop convergence dynamic. Finally, Section 6 summarises the main conclusions of the study and highlights potential directions for future research.

2. Problem formulation and analytical description

This section introduces the mathematical formulation of the optimal controller tuning problem. The objective is to determine a set of controller parameters that minimise the deviation between the actual closed-loop response of a nonlinear system and a predefined target response. To this end, the system dynamics, the controller structure, and the optimisation problem governing the tuning process are defined.

2.1. Nonlinear system model

Consider a nonlinear dynamical system $\mathcal{S}$ described by the state–space representation

$$\mathcal{S} \equiv \begin{cases} \dot{x}(t) = f(x(t), u(t)) \\ y(t) = g(x(t), u(t)) \end{cases} \tag{1}$$

where $x(t) \in \mathbb{R}^s$ represents the system state vector, $u(t) \in \mathbb{R}^m$ is the control input vector, and $y(t) \in \mathbb{R}^p$ denotes the system output vector. The function $f : \mathbb{R}^s \times \mathbb{R}^m \to \mathbb{R}^s$ characterises the system dynamics, while $g : \mathbb{R}^s \times \mathbb{R}^m \to \mathbb{R}^p$ defines the system output mapping. The function $f(\cdot)$ exhibits the nonlinearities of the system. It is assumed that the system is both controllable and observable under a suitable choice of control input. It must be noted that, although the formulation is presented for a general multi-input, multi-output (MIMO) system, the focus of this work, particularly in the application case in Section 4, will be on single-input, single-output (SISO) system. The application to MIMO systems follows naturally from the presented methodology.

2.2. Parameterised controller

The control input $u(t)$ is generated by a parameterised controller $\mathcal{S}_\mathcal{K}$, which is itself a dynamical system with the state–space representation

$$\mathcal{S}_\mathcal{K} \equiv \begin{cases} \dot{x}_k(t) = f_k(x_k(t), e(t), \Theta) \\ u(t) = g_k(x_k(t), e(t), \Theta) \end{cases} \tag{2}$$

In Eq. (2), $x_k(t) \in \mathbb{R}^q$ denotes the internal state of the controller, while $e(t) = r(t) - y(t)$ represents the control error, defined as the difference between a reference input $r(t) \in \mathbb{R}^p$ and the system output $y(t) \in \mathbb{R}^p$. The vector $\Theta \in \mathbb{R}^n$ comprises the 'tunable' controller parameters. The function $f_k : \mathbb{R}^q \times \mathbb{R}^p \times \mathbb{R}^n \to \mathbb{R}^q$ characterises the controller dynamics, while $g_k : \mathbb{R}^q \times \mathbb{R}^p \times \mathbb{R}^n \to \mathbb{R}^m$ defines the control law.

The controller structure is not restricted to a specific form and may encompass linear, nonlinear, or adaptive control strategies, such as proportional–integral–derivative (PID) controllers, sliding mode controllers, or model-based optimal controllers.

2.3. Target closed-loop behaviour

To define an optimal tuning criterion, the key variable of interest is the target $y_d(t)$, which represents the desired closed-loop behaviour of the controlled system. The goal is for the controlled system to exhibit this target output when subject to a reference excitation. To achieve this, a system $\mathcal{S}_d$ is proposed, which models the evolution of the target output $y_d(t)$. While the specific formulation of the target system can vary, the important consideration is that the system should be designed to produce the desired output signal $y_d(t)$. The system $\mathcal{S}_d$ can be defined using nonlinear dynamics, offering the flexibility to specify more complex closed-loop behaviours, though the approach is not restricted to this formulation. The general formulation of the target system $\mathcal{S}_d$ is given by:

$$\mathcal{S}_d \equiv \begin{cases} \dot{x}_d(t) = f_d(x_d(t), w(t)), \\ y_d(t) = g_d(x_d(t), w(t)), \end{cases} \tag{3}$$

where the dynamics of the system $\mathcal{S}_d$ are defined by f_d and g_d, with the primary focus being on the output $y_d(t)$. It is assumed that the system $\mathcal{S}_d$ exhibits well-defined stability properties, ensuring that the output $y_d(t)$ remains stable and converges to the desired behaviour. However, for simplicity and tractability, a linear target system can be employed as a specific case. In this linear case, the target system is represented by the linear time-invariant (LTI) state–space model:

$$\mathcal{S}_d \equiv \begin{cases} \dot{x}_d(t) = A_d x_d(t) + B_d w(t), \\ y_d(t) = C_d x_d(t), \end{cases} \tag{4}$$

where $A_d \in \mathbb{R}^{n_d \times n_d}$, $B_d \in \mathbb{R}^{n_d \times 1}$, and $C_d \in \mathbb{R}^{p \times n_d}$ define the dynamics of the target system. The input $w(t)$ is an external excitation signal, which can be chosen as a unit step function (Heaviside step), which generates the desired closed-loop response. The matrix A_d is assumed to be Hurwitz, ensuring that the response is stable. A particularly useful target response in many practical applications is the exponential convergence to a steady-state value, which, assuming $t \geq 0$, can be represented as:

$$y_d(t) = 1 - e^{-\alpha t}\cos(\omega t), \quad \alpha > 0, \quad \omega \geq 0. \tag{5}$$

This formulation covers both overdamped and underdamped behaviours, where α governs the decay rate and ω determines the oscillatory nature of the response. The case when $\omega = 0$ corresponds to a purely exponential decay, given by:

$$y_d(t) = 1 - e^{-\alpha t}, \quad \alpha > 0. \tag{6}$$

This is a common approximation used for first-order system responses. The optimisation process is aimed at ensuring that the controlled response of the system, when subjected to a step input, closely matches the prescribed exponential convergence behaviour. However, this

framework is flexible and can accommodate more general target responses, as long as the system exhibits well-defined stability and convergence properties. Finally, in the context of the exponential case, an exponential convergence condition can be established for the error $e_c(t)$, which represents the difference between the actual and desired system responses. Thus, the optimisation procedure seeks to ensure that the error behaves as follows:

$$e_c(t) \leq Me^{-\alpha t}, \tag{7}$$

where M is a constant, and α is the decay rate. This condition guarantees that the error converges to zero with exponential decay, ensuring that the behaviour of the controlled system closely matches the desired target response.

2.4. Optimisation framework for controller tuning

The tuning process is formulated as an optimisation problem in which the goal is to find the optimal parameter vector Θ^* that minimises the deviation between the actual system output $y(t)$ and the target response $y_d(t)$. This objective is mathematically expressed as

$$\Theta^* = \arg\min_{\Theta} J(\Theta), \tag{8}$$

where the cost function $J(\Theta)$ quantifies the error between the actual and target responses. A typical choice is the least-squares error criterion

$$J(\Theta) = \int_0^T \left(y_d(t) - y(t)\right)^2 dt. \tag{9}$$

The optimisation is subject to constraints on the controller parameters, which can be classified as linear constraints of the form

$$A\Theta \leq b, \tag{10}$$

which may encode parameter limits, gain restrictions, or robustness margins, or nonlinear constraints of the form

$$c(\Theta) \leq 0, \tag{11}$$

such as the conditions required for stability and robustness of the SMC. The presence of nonlinear constraints generally leads to a nonconvex optimisation problem, requiring numerical solvers for its solution.

2.5. Considerations on numerical implementation

Since system $\mathcal{S}$ is nonlinear, solving the optimisation problem in Eq. (8) requires the numerical simulation of the closed-loop dynamics for each candidate Θ. Due to potential '*nonsmooth*' behaviour, such as discontinuities arising in SMC, numerical solvers designed for stiff systems, such as `ode23s` or `ode15s`, are preferred over higher-order methods that rely on smooth trajectories, as they offer better stability and efficiency when handling rapid transients (The MathWorks, 2023b). In general, for smooth scenarios, solvers like `ode45`, based on the Runge–Kutta method, can be effectively applied (The MathWorks, 2023b).

Furthermore, given the nonconvex nature of $J(\Theta)$, local gradient-based methods may not be sufficient to guarantee convergence to a globally optimal solution (SciPy Community, 2023; The MathWorks, 2023a) Consequently, global optimisation techniques such as pattern search or genetic algorithms are employed to explore the parameter space more effectively. Several numerical optimisation solvers can be used for this purpose, including the one employed in this study (The MathWorks, 2023a). To ensure practical implementability, additional constraints on the controller parameters are imposed, restricting Θ within a feasible range,

$$\Theta \in [\Theta_{\min}, \Theta_{\max}]. \tag{12}$$

To illustrate the overall implementation of the proposed tuning methodology, Fig. 1 presents a high-level scheme of the complete offline procedure. The flowchart in Fig. 1 outlines a structured, three-layer framework for the offline tuning and validation of control strategies. Layer 3 involves the initialisation of all system components, including the plant and controller models, numerical solvers, optimisation constraints, and target dynamics. It also defines the global optimisation algorithm (e.g., particle swarm, genetic algorithms, pattern search, etc.) and simulation settings. Layer 2 contains the core optimisation loop, where successive controller parameter sets are evaluated by repeatedly calling the objective function. This function executes a closed-loop simulation (handled in Layer 1), computes the tracking error or sliding surface, depending on the considered control scheme, with respect to the reference signal, and returns a scalar performance metric to guide the optimiser. The process continues until a stopping criterion is satisfied. Layer 1 performs the closed-loop simulations and post-optimisation validations using the optimal controller. The method clearly separates tuning from deployment, highlighting its offline nature and ensuring that performance is assessed only after the optimisation phase has concluded. Additionally, optional elements, such as the optimisation constraints highlighted by the dashed red line in Fig. 1, may be incorporated in specific implementations. Generally, optimisation parameters can be bounded, and nonlinear constraints can be imposed to ensure analytical finite-time convergence conditions for nonlinear control schemes using this set of constraints.

3. Considered control structures

In this section, two control schemes are selected to illustrate the reach of the proposed optimisation-based tuning methodology. While the methodology itself is not constrained to a specific control structure, the chosen schemes encompass key requirements commonly encountered in control design.

The first control scheme considered is the PI controller (Section 3.1), a widely accepted approach in industry, academia, and educational environments. As a particular case within a broader family of nonlinear controllers, the PI scheme benefits from systematic tuning procedures, which can be guided by empirical rules or analytical methods, such as pole placement. Moreover, in general real-world applications, given a predefined steady-state error tolerance, the controller can be tuned to ensure convergence within the desired bounds.

The second scheme involves a super-twisting SMC (Section 3.2), a robust nonlinear control strategy particularly suited for systems with significant uncertainties and modelling errors. In addition, SMC are well-established within the control community. Unlike other nonlinear control techniques, such as backstepping or feedback linearisation, which require precise model knowledge to implement the necessary diffeomorphism in the feedback path (Khalil, 1996; Slotine et al., 1991), sliding mode control remains effective under model uncertainties. Within this framework, second-order sliding mode algorithms, such as the super-twisting approach, provides a smooth control action that mitigates the chattering effects, typically observed in first-order implementations, making it more feasible for practical applications.

3.1. Proportional-integral controller

A widely used control strategy for systems requiring compensation of steady-state errors is the PI controller. The PI control law in the time domain is given by

$$u(t) = K_1 e(t) + K_2 \int_0^t e(\tau) d\tau + u_{eq}, \tag{13}$$

where K_1 and K_2 are the proportional and integral gains, respectively, and $e(t)$ is the error signal, defined as the difference between the output $y(t)$ and the reference $r(t)$, i.e., $e(t) = r(t) - y(t)$ (see Goodwin et al., 2001 for a detailed discussion of P, PI, as in Eq. (13), and PID controllers, as well as polynomial control approaches in general). The term u_{eq} represents the equilibrium control trajectory term, which ensures that

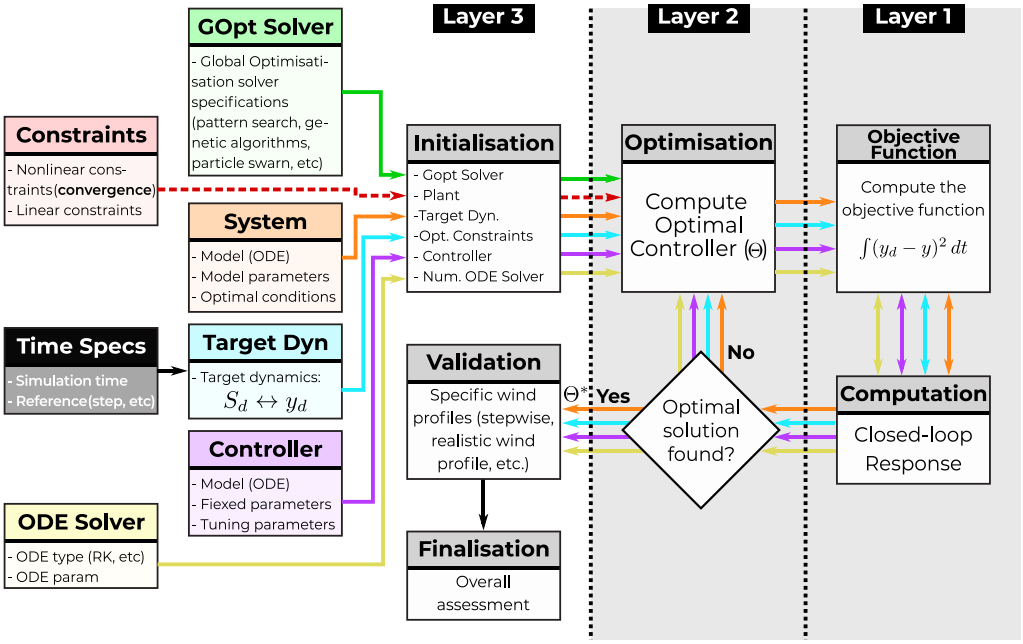

Fig. 1. Flowchart of the offline controller tuning framework, organised in three layers: initialisation (Layer 3), iterative optimisation (Layer 2), and closed-loop simulation and validation (Layer 1). The scheme emphasises the fully offline nature of the approach. The dashed red line represents an optional interaction used, for example, in the definition of constraints. (For interpretation of the references to colour in this figure legend, the reader is referred to the web version of this article.)

the system remains at the desired operating point. This term is crucial for maintaining the steady-state performance of the system, particularly in ensuring that the system output stabilises at the desired value[1].

To express the PI controller in a state–space form, an auxiliary state variable $x_k(t)$, representing the integral of the error, is introduced:

$$\dot{x}_k(t) = e(t), \quad u(t) = K_1 e(t) + K_2 x_k(t) + u_{eq}. \tag{14}$$

In this formulation, the controller state vector is $x_k(t) \in \mathbb{R}$, and the dynamics of the controller are defined by:

$$f_k(x_k, e, \Theta) = e, \tag{15}$$

where f_k represents the evolution of the auxiliary state $x_k(t)$.

The control law is given by:

$$g_k(x_k, e, \Theta) = K_1 e + K_2 x_k + u_{eq}, \tag{16}$$

where g_k defines the control output in terms of the state variables and the tuning parameters K_1 and K_2.

The parameter vector for the PI controller is then given by:

$$\Theta = \begin{bmatrix} K_1 \\ K_2 \end{bmatrix} \in \mathbb{R}^2.f \tag{17}$$

3.2. Super-twisting sliding mode controller (STSMC)

The STSMC is a robust and nonlinear control law designed to drive a sliding variable $\sigma(t)$ of relative degree one and its first time derivative to zero in finite time, thereby ensuring that the system state follows the desired trajectory despite model uncertainties and external disturbances (Fridman et al., 2015; Shtessel et al., 2014). In SMC the variable $\sigma(t)$ (often referred to as the sliding function) is typically constructed as a linear or nonlinear combination of measurable system states. It is usually defined as a tracking error or a function tailored to encode the control objectives. STSMC can also be interpreted as a nonlinear PI control strategy, the control action enforces convergence to the sliding manifold or surface ($\sigma(t) = \dot{\sigma}(t) = 0$) in higher-order SMC schemes such as STSMC, exhibiting strong robustness features. The dynamics of the sliding variable for a generic system are typically expressed as:

$$\dot{\sigma}(t) = h(x(t)) + \phi(x(t))u(t), \tag{18}$$

where h and ϕ are unknown functions of the state of the system $x(t)$ with bounded derivatives, and $u(t)$ is the control input.[2]

The super-twisting control law is given by Shtessel et al. (2014):

$$u = u_1 + u_2 + u_{eq}, \tag{19}$$

where, starting with u_1 for simplicity,

$$u_1 = -K_1 |\sigma|^{\frac{1}{2}} \operatorname{sign}(\sigma), \tag{20}$$

with K_1 is a positive constant that regulates the convergence rate, $|\sigma(t)|^{\frac{1}{2}}$ modulates the control effort to reduce chattering, and u_2 is an auxiliary control term ensuring smooth control action, and finally, in Eq. (19), u_{eq}, is the equilibrium trajectory, introduced in Eq. (13). The dynamics of u_2 are given by:

$$\dot{u}_2 = \begin{cases} -u, & \text{if } |u| > U_M, \\ -K_2 \operatorname{sign}(\sigma), & \text{if } |u| \le U_M, \end{cases} \tag{21}$$

where U_M is a saturation limit and K_2 is a positive constant determining the convergence speed when $|u| \le U_M$. To express the STSMC in a state–space form, an auxiliary state variable $x_k(t)$, representing u_2, is introduced:

$$\dot{x}_k = \begin{cases} -(x_k - K_1 |\sigma|^{\frac{1}{2}} \operatorname{sign}(\sigma)), & \text{if } \Delta > U_M, \\ -K_2 \operatorname{sign}(\sigma), & \text{if } \Delta \le U_M, \end{cases} \tag{22}$$

[1] The signal u_{eq} is sometimes referred to as the equilibrium or nominal term in control literature, as it represents the steady-state value required to maintain the desired operating point of the system.

[2] From now on, the dependence on time t is omitted when clear from the context.

where $\Delta = |x_k - K_1|\sigma|^{\frac{1}{2}} \operatorname{sign}(\sigma)|$. Thus, in the parameterised controller framework, the controller dynamics are given by:

$$f_k(x_k, e, \Theta) = \begin{cases} -(x_k - K_1|\sigma|^{\frac{1}{2}} \operatorname{sign}(\sigma)), & \text{if } \Delta > U_M, \\ -K_2 \operatorname{sign}(\sigma), & \text{if } \Delta \leq U_M. \end{cases} \tag{23}$$

The output mapping $g(\cdot)$ is expressed as

$$g_k(x_k, e, \Theta) = x_k - K_1|\sigma|^{\frac{1}{2}} \operatorname{sign}(\sigma) + u_{eq}, \tag{24}$$

which includes the equilibrium control trajectory term, introduced in Eq. (19).

The overall control input can then be written as:

$$u(t) = u_1(t) + u_2(t) + u_{eq}, \tag{25}$$

where $u_1(t)$ represents the proportional action, $u_2(t)$ is the integral (super-twisting) component, and u_{eq} is the equilibrium control trajectory term (see Eq. (13)).

The parameter vector Θ is defined as:

$$\Theta = \begin{bmatrix} K_1 \\ K_2 \\ U_M \end{bmatrix} \in \mathbb{R}^3, \tag{26}$$

where K_1 and K_2 regulate the convergence rate and smoothness of the control law, while U_M serves as an additional tuning parameter controlling the saturation threshold. However, U_M can be fixed based on system constraints or prior knowledge, in which case it is removed from the set of tuning parameters, reducing Θ to a two-dimensional vector:

$$\Theta = \begin{bmatrix} K_1 \\ K_2 \end{bmatrix} \in \mathbb{R}^2, \tag{27}$$

as considered in the application case in Section 4.

Based on standard results in the sliding mode control literature, the following assumptions are required to ensure finite-time convergences, stability, and robustness:

$$|\dot{h}(x)| + |\dot{\phi}(x)|\, U_M \leq C, \tag{28}$$

$$0 \leq K_m \leq \phi(x) \leq K_M, \tag{29}$$

$$|h(x)| < q|\phi(x)|U_M, \quad q \in (0, 1), \tag{30}$$

where C, K_m, K_M, and q are constants that define system robustness. From the assumptions in Eqs. (28), (29), and (30), and following the results presented in Shtessel et al. (2014), it is possible to derive explicit sufficient conditions that ensure finite-time convergence of the STSMC. These conditions, typically nonlinear inequalities involving the gains and system bounds (e.g., K_m, K_M, C, and q), are well-established in the literature and can be directly applied to validate the stability of a given gain configuration. However, in this study, these convergence conditions are not embedded in the optimisation to avoid prematurely restricting the parameter search space. This allows broader exploration during tuning. Final gains are verified a *posteriori* to ensure they meet the theoretical stability requirements. It is also worth noting that, in practical applications, such nonlinear constraints, if desired, can be readily integrated into most global optimisation frameworks, such as those available in MATLAB (The MathWorks, 2023a) or Python (SciPy Community, 2023). Therefore, although these constraints are omitted in the application case presented here to highlight methodological flexibility, they can be seamlessly incorporated in other implementations if required.

3.2.1. Implementation in this study

In this work, the sliding variable σ is defined using the error:

$$\sigma(t) = e(t) = r(t) - y(t), \tag{31}$$

where $r(t)$ is the reference trajectory and $y(t)$ is the actual output of the system.

For a comprehensive discussion on sliding mode control and super-twisting control, the interested reader is referred to Fridman et al. (2015), Shtessel et al. (2014).

4. Application case: Wind turbine control

To validate the tuning methodology presented in this work, a model describing the dynamic behaviour of the wind energy conversion system (WECS), as detailed in Section 4.1, is considered. This model captures the key aerodynamic and electromechanical interactions, including the turbine dynamics, generator characteristics, and control actions applied to the system. The wind conditions driving the system are characterised in Section 4.2, providing a realistic representation of the turbulent wind field acting on the turbine rotor. A comprehensive simulation framework, as presented in Section 4.3, is considered for the evaluation and validation of the proposed tuning approach under realistic operating scenarios. Finally, the results obtained with the PI and the STSMC are presented in Sections 4.4 and 4.5, respectively.

4.1. The wind turbine model

This study considers a variable-speed wind turbine connected to the grid through a doubly-fed induction generator (DFIG) operating in a static Kramer drive topology. A comprehensive electromechanical description of the system can be found in Evangelista et al. (2013). In this configuration, the stator directly injects power into the grid, and additionally, a fraction of the rotor power is recovered via an electronic converter composed of an uncontrolled rectifier bridge, a ripple-smoothing inductor, and a controlled rectifier acting as an inverter. The generator torque and, consequently, the operating speed of the turbine can be regulated by adjusting the firing angle δ in the rectifier of the converter. This topology enables variable-speed operation while maintaining a grid-synchronised frequency, reduces the required power electronics rating by processing only the recovered rotor power, and allows for precise control of the generator torque (Baroudi et al., 2007a; Spée et al., 1995). The wind energy conversion system analysed in this study is selected to provide a representative and industrially relevant application context for evaluating the proposed tuning algorithm. Among the different technologies deployed in the wind energy sector, the DFIG remains one of the most widely used due to its capability for variable-speed operation while maintaining grid-synchronous frequency. DFIG-based configurations with partial-scale power electronics represent a well-established topology in medium-scale wind farms (Baroudi et al., 2007b; Bianchi et al., 2007; Bose, 2002; Munteanu et al., 2008). The specific system adopted in this work is based on the static Kramer drive, which allows for partial rotor power recovery and can be effectively modelled as a single-input, single-output system. This characteristic simplifies the implementation of both linear and nonlinear control strategies (De Battista et al., 2001; Evangelista et al., 2010a, 2010b; Mayosky & Cancelo, 1999; Puleston et al., 2000). Although less common in modern commercial deployments, the static Kramer drive remains a cost-effective and technically instructive configuration, with practical relevance in legacy and research-oriented setups. Moreover, since the generator torque remains within rated limits and the primary aim is to assess control performance, a simplified model is adopted, following prior works (Evangelista et al., 2013). Overall, the selected configuration provides a meaningful platform to demonstrate the capabilities of the proposed tuning method. Thus, the adopted model belongs to a class of control-oriented wind turbine representations that balance physical fidelity with analytical tractability. Such models are standard in the wind energy control literature and are frequently used to test and compare advanced control strategies before transitioning to full-order aeroelastic simulators (Bianchi et al., 2007; Boersma et al., 2017; Evangelista et al., 2013). This intermediate level of complexity is particularly suited for developing and validating tuning methodologies, as it preserves the key nonlinear dynamics and performance-relevant interactions of the turbine-generator system.

Operating regions

Wind turbine operation is typically divided into four regions, each associated with different control objectives and energy conversion strategies (Bianchi et al., 2007; Burton et al., 2011). At low wind speeds, the turbine remains idle as the available power is insufficient to overcome mechanical losses. Once wind speed exceeds the cut-in threshold, the system enters the partial-load region, where the turbine adjusts its rotational speed to maintain the optimal tip-speed ratio $\lambda^\star$, maximising the aerodynamic efficiency. In the full-load region, the extracted power is limited to its rated value to prevent mechanical and electrical overload, typically via pitch control. Finally, at excessively high wind speeds, the turbine is shut down to avoid structural damage. For this study, the second region (partial-load region) is considered for the application case, as described in the following[3].

For optimal energy extraction in the partial-load region, the turbine rotational speed tracks the reference speed

$$\Omega_{\text{ref}}(t) = r(t) = \frac{\lambda^\star}{R} v(t), \tag{32}$$

where v is the wind speed and R is the rotor radius. The extracted power is given by

$$P_t = \frac{1}{2}\pi\rho R^2 C_p(\lambda) v^3, \tag{33}$$

where ρ is the air density, and $C_p(\lambda)$ is the power coefficient, which quantifies the efficiency of the turbine in converting wind energy into mechanical power. This coefficient depends on the tip-speed ratio, defined as

$$\lambda = \frac{\Omega R}{v}. \tag{34}$$

The aerodynamic torque exerted on the rotor is given by

$$T_t = \frac{1}{2}\pi\rho R^3 C_t(\lambda) v^2, \tag{35}$$

where $C_t(\lambda)$, the torque coefficient, is related to the power coefficient as

$$C_t(\lambda) = \frac{C_p(\lambda)}{\lambda}. \tag{36}$$

Thus, while $C_p(\lambda)$ characterises power extraction efficiency, $C_t(\lambda)$ represents how the aerodynamic torque varies with the tip-speed ratio. In this study, $C_t(\lambda)$ is approximated using a third-order polynomial:

$$C_t(\lambda) = \max\left(0, c_3\lambda^3 + c_2\lambda^2 + c_1\lambda + c_0\right), \quad 0 < \lambda < 500, \tag{37}$$

where the range $0 < \lambda < 500$ is chosen to ensure consistency with the wind turbine model under consideration (Evangelista et al., 2013). The max operator guarantees a non-negative approximation of C_t, preserving the physical meaning of this coefficient in the characterisation of wind energy systems. This approximation ensures smooth variation across the relevant operating range, enabling efficient modelling of turbine dynamics.

The system dynamics are governed by Newton's second law and can be expressed in state–space form as:

$$\frac{d\Omega}{dt} = \frac{1}{J}(T_t + T_e), \tag{38}$$

where Ω is the rotational speed (state variable), T_t is the aerodynamic torque as defined in Eq. (35), and T_e is the generator torque. The parameter J represents the total inertia of the rotating components. Eq. (38) thus represents a first-order state–space model of the rotational dynamics of the wind turbine. To complete the definition in Eq. (38), the generator torque follows

$$T_e = \frac{3V_s^2 p\, n}{\omega_s R_b} u + \frac{3V_s^2 p}{\omega_s R_b}\left(1 - \frac{p\,\Omega}{\omega_s}\right), \tag{39}$$

[3] For the model described in the following, a rigid drive train is assumed, and all turbine variables are referred to the fast shaft (or generator side) by applying the transmission ratio k_{gb} of the gearbox (see Table 1).

Table 1
Wind turbine and generator parameters.

Symbol	Value	Description
p	2	Generator pole pairs
f_s	50 Hz	Electrical frequency
ω_s	$2\pi f_s$ rad/s	Stator field angular speed
V_s	460 V/$\sqrt{3}$	Phase voltage RMS
n_1	1.2	Stator-to-rotor turns ratio
n_2	1.2	Stator-to-inverter turns ratio
n	n_1/n_2	Transformer turns ratio
R_r	0.238 Ω	Rotor resistance (stator side)
R_f	0.0259 Ω	DC link resistance
R_b	$R_r + 0.55R_f$	Nominal resistance
R	6.75 m	Blade radius
k_{gb}	19.85	Gearbox transmission ratio
$J_t^\star$	2237.65 kg m^2	Inertia of the turbine rotor (turbine side)
J_t	5.679 kg m^2	Inertia of the turbine rotor (generator side)
J_g	1.3833 kg m^2	Inertia of generator rotating parts
J	$J_t/k_{gb}^2 + J_g$	Total inertia
ρ	1.2242 kg/m^3	Air density
$C_t(\lambda)$	$c_3 = 1.191 \times 10^{-9}$	Turbine torque coefficient (polynomial coefficients):
	$c_2 = -1.03 \times 10^{-6}$	
	$c_1 = 2.214 \times 10^{-4}$	
	$c_0 = -1.142 \times 10^{-2}$	

The variables are referenced to the generator side as follows: $T_t = \frac{T_t^\star}{k_{gb}}$ and $\Omega = \Omega_t^\star k_{gb}$, where the superscript $\star$ denotes the values at the turbine side, where k_{gb} denotes the transmission ratio of the gearbox.

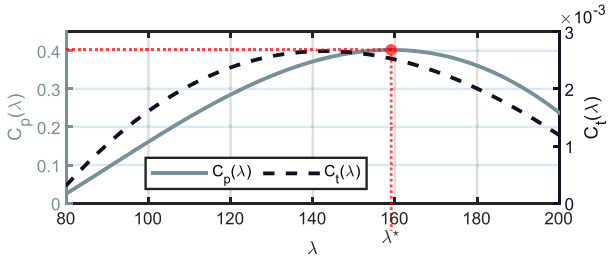

Fig. 2. Characteristic curves of $C_t(\lambda)$ and $C_p(\lambda)$, as functions of λ. The values of λ on the x-axis are referenced to the generator side, while for the turbine side, $\lambda^\star = \lambda/k_{gb}$. $C_p(\lambda)$ exhibits a unique maximum at λ_{opt}, corresponding to the most efficient energy conversion point.

where, $u = |\cos(\delta)|$ represents the control input, which modulates the generated torque. The model parameters, summarised in Table 1, define the electrical and mechanical characteristics of the turbine-generator system. This framework serves as the basis for designing and evaluating control strategies aimed at optimising energy conversion efficiency in variable-speed operation.

Fig. 2 shows the resulting $C_t(\lambda)$ and $C_p(\lambda)$ curves, indicating the location of $\lambda^\star = 159.01$, corresponding to the maximum C_p. In Fig. 2, the values of λ on the x-axis are referenced to the generator side, while for the turbine side, $\lambda^\star = \lambda/k_{gb}$.

It is important to note that, although the model used in this study is based on a DFIG with a static Kramer drive, the proposed tuning methodology is not limited to this configuration. The approach generalises to a broad class of systems, including, but not limited to, wind turbines. As such, the selected model serves as a representative but non-restrictive platform to illustrate the tuning process, allowing for clear exposition of the methodology without loss of generality. This model-agnostic nature is particularly relevant for practical deployment across diverse turbine architectures.

4.2. Wind field model

The wind profile is generated using a stochastic model based on the Kaimal spectrum (Kaimal et al., 1972), which defines turbulence characteristics following the IEC 61400-1 standard (International Electrotechnical Commission, 2019). The longitudinal wind fluctuations are modelled through the power spectral density (PSD):

$$S_u(f) = \frac{4\sigma_u^2 L}{U} \frac{1}{(1 + 6fL/U)^{5/3}} \tag{40}$$

where σ_u is the turbulence intensity, L the turbulence length scale, U the mean wind speed, and f the frequency. This formulation captures both low-frequency variations and high-frequency turbulence, ensuring consistency with real wind conditions.

To generate a time-domain wind profile, a spectral synthesis approach is employed:

1. A frequency representation is defined based on the simulation parameters.
2. The Kaimal spectrum is applied to shape the turbulence characteristics.
3. Random phase components ensure a stochastic nature.
4. An inverse Fourier transform reconstructs the wind fluctuations.
5. The resulting signal is adjusted to match the desired mean wind speed.

This ensures a realistic wind profile consistent with observed turbulence properties (Stull, 2012). An example of a wind profile obtained with $\sigma_u = 1$ m/s (moderate turbulence), $L = 500$ m (large-scale turbulence structures), and a mean wind speed of 10 m/s is shown in Fig. 3. The Kaimal spectrum-based turbulence model used here, together with spectral synthesis and moderate turbulence intensity, is consistent with IEC 61400-1 recommendations (International Electrotechnical Commission, 2019) and reflects typical offshore or coastal wind resource conditions. This modelling approach provides inflow dynamics that are both stochastic and representative of realistic industrial scenarios. While the tuning methodology is developed using an analytical model, it is validated within a more complete and realistic simulation framework, consistent with industry practices. The simulation incorporates stochastic wind inflow generated from the Kaimal turbulence spectrum, an appropriate solver and integration method, and realistic turbine and generator parameters. Initial simulation tests are conducted using stepped wind profiles, which facilitate a clearer visualisation and evaluation of the dynamic response of the system under the controller gains obtained from the proposed tuning method. Subsequently, the wind inflow model is refined to incorporate turbulence characteristics derived from the Kaimal spectrum and wind profiles compliant with IEC standards, parameterised for a representative geographic location. By selecting a low-turbulence case ($\sigma_u = 1$ m/s), the simulated wind fields align with conditions typically observed in stable atmospheric boundary layers over large water bodies or coastal plains. The scenario depicted in Fig. 3 is characteristic of offshore and coastal environments with moderate wind variability and low turbulence intensity (Burton et al., 2011; Stull, 2012). Such conditions are commonly found in regions like the Argentine Sea near Patagonia, where the atmospheric boundary layer remains relatively stable (Guozden et al., 2018; Labriola, 2020).

4.3. Assessment setup

The assessment is structured into two main subsections, each focusing on the performance of one of the controllers: the PI controller and the Super Twisting SMC. Both controllers, whose frameworks are outlined in Section 3, regulate the system output $\Omega(t)$, which corresponds to the variable $y(t)$ in Eq. (1). The system responses obtained with the PI and SM controllers are denoted as $\Omega_{\text{PI}}(t)$ and $\Omega_{\text{SM}}(t)$, respectively. To

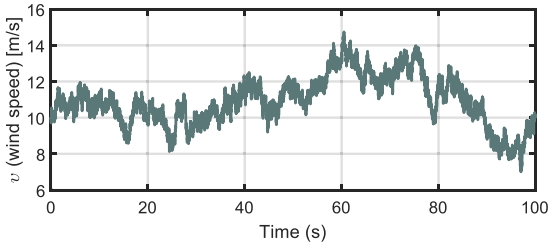

Fig. 3. Synthetic wind speed profile generated based on the Kaimal turbulence model, representing a moderate turbulence scenario with $\sigma_u = 1$, a length scale of $L = 500$ m, and a mean wind speed of $U = 10$ m/s. This profile is used to simulate realistic inflow conditions for the wind energy system.

maintain consistency with the specific application, the variables $y_d(t)$ and $w(t)$, introduced in Eq. (3), are referred to as $\Omega_d(t)$ and $\Omega_w(t)$, respectively, in the tuning process results, where $\Omega_d(t)$ defines the target dynamic.

The tuning process aims to shape the closed-loop response based on predefined target behaviours, considering two distinct reference responses: an exponential response and a ramp response. The exponential response, introduced in Eq. (5), is characterised by variations in the decay rate α and oscillation frequency ω. On the other hand, the ramp response follows a segmented structure: starting at the initial condition, transitioning through a linear increase over the time interval t_e, and ultimately stabilising at a constant final value. Thus, the exponential response is given by:

$$\Omega_{\text{d}}(t) = \begin{cases} \Omega_{\text{ini}}, & t \le t_c, \\ \Omega_{\text{ini}} + (\Omega_{\text{end}} - \Omega_{\text{ini}}) \left(1 - e^{-\alpha(t-t_c)}\right. & \\ \left. \times \cos(\omega(t - t_c))\right), & t > t_c. \end{cases} \tag{41}$$

where t_c represents the step change time, and the damping and oscillatory behaviour are governed by the real and imaginary components of $\alpha + \jmath\omega$, while Ω_{ini} and Ω_{end} are the initial and final reference values. Similarly, for the ramp reference trajectory, the reference remains constant at Ω_{ini} for $t \le t_c$, transitions linearly from Ω_{ini} to Ω_{end} with a slope of $\frac{\Omega_{\text{end}} - \Omega_{\text{ini}}}{t_e}$ during $t_c < t \le t_c + t_e$, and stabilises at Ω_{end} for $t > t_c + t_e$. This is represented by:

$$\Omega_d(t) = \begin{cases} \Omega_{\text{ini}}, & t \le t_c, \\ \Omega_{\text{ini}} + \dfrac{\Omega_{\text{end}} - \Omega_{\text{ini}}}{t_e}(t - t_c), & t_c < t \le t_c + t_e, \\ \Omega_{\text{end}}, & t > t_c + t_e. \end{cases} \tag{42}$$

The motivation for incorporating the exponential response arises from its status as a well-established benchmark in control theory, offering a clear reference for performance assessment in linear systems. In contrast, the ramp response is chosen because it reflects the finite-time convergence characteristics typical of SMC strategies, while preserving a response that qualitatively aligns with the piecewise continuous trajectories often observed in SMC. This dual approach, based on the considered exponential and ramp signals, enables a more comprehensive evaluation, highlighting the natural strengths and limitations of both PI and SM controllers in their respective dynamic contexts.

To thoroughly evaluate both controllers under various conditions, three main **assessment scenarios** are considered:

- **Scenario 1: Response to exponential and ramp references.** This scenario evaluates the ability of the controllers to track predefined closed-loop behaviours, using both exponential and ramp responses. For the optimisation-based tuning procedure presented in this section, an initial wind speed of $v_{\text{ini}} = 10$ m/s is considered, followed by a 10% variation, resulting in a final wind speed of 11 m/s. This variation corresponds to rotational speeds of

$\Omega_{\text{ini}} = 235.70$ rad/s, and $\Omega_{\text{end}} = 259.27$ rad/s, respectively, given the optimal tip-speed ratio $\lambda^\star$ and wind turbine radius R (see Table 1 and Fig. 2). The wind speed value is selected following the nominal wind turbine characteristics. In this scenario, the following parameter ranges are considered for the exponential and ramp responses: $\alpha \in \{1, 2, 5, 15\}$, $\omega \in \{1, 2, 5, 15\}$, and t_e, for the ramp response, $\in \{0.25, 5, 10, 12\}$. Additionally, $t_c = 0.1$ s. This setup ensures that a comprehensive range of tuning parameters is explored to assess the performance of the controllers under various conditions.

- **Scenario 2: Response to stepwise wind speed variations.** In this scenario, the controllers are tested through a series of stepwise changes in the reference signal $\Omega_{\text{ref}}(t)$, spanning the dynamic range of wind speeds from 8 m/s to 12 m/s. The objective is to assess the transient response of the closed-loop system and evaluate the ability of the controllers to handle abrupt shifts across an extended dynamic range. The system response is analysed by tuning the controllers based on the exponential target response for various values of $\alpha \in \{5, 10\}$ while keeping $\omega = 0$, enabling a systematic comparison of performance variations.
- **Scenario 3: Response under a realistic wind profile.** This scenario evaluates the ability of the controllers to track a wind profile synthesised as outlined in Section 4.2, which includes both steady and turbulent wind components. The reference trajectory $\Omega_{\text{ref}}(t)$ simulates realistic wind fluctuations (rotational velocity) over a 50-second period. The performance is assessed by tuning the controllers based on the exponential target response for $\alpha \in \{5, 20\}$ while maintaining $\omega = 0$. This allows for a detailed comparison of how the controllers handle the trade-off between tracking accuracy and closed-loop filtering, especially in the presence of high-frequency fluctuations in the wind profile.

To enhance clarity in the visual representation of results, some plots adopt a 'neutral red' legend for general line styles, while specific colours are applied directly in the figures. This strategy reduces redundancy while maintaining visual consistency.

For the SM controller, the nonlinear finite-time convergence constraint, derived from Eqs. (28), (29), and (30), are intentionally excluded during the initial search phase. This decision aims to enable the optimisation algorithm to freely explore the parameter space, without prematurely restricting the search to regions that strictly satisfy the convergence conditions. As a result, the parameters K_m, K_M, and C, which are directly linked to the aforementioned equations, are not enforced at this stage of the tuning process. However, before accepting a final solution, the obtained parameters are verified to ensure they remain within the theoretical framework of the controller, preserving the necessary conditions for stability and robustness. This approach is considered to fully validate the exploration capability of the tuning algorithm, although, in more rigorous implementations, these constraints can be directly incorporated into the optimisation problem. It is worth noting that, in the vast majority of practical SM controller implementations, a final manual tuning step, often based on simulations, is applied, which may result in parameter selections that lie even outside the theoretical regions for robustness and stability due to the conservativeness of such constraints. However, this discussion is beyond the scope of this study, which focuses on the tuning methodology and its consequences on closed-loop dynamics. Finally, the variable U_M in Eq. (21) is set to 1, reflecting the theoretical and practical upper bound of the control input $u = |\cos(\delta)|$, which remains strictly below 1 due to the operational range of the firing angle $\delta \in (90°, 180°)$ in the considered inverter-based topology (Cadirci & Ermis, 1992; Puleston et al., 2000).

Assessment setup and target closed-loop behaviour summary

To summarise, the closed-loop behaviour is implicitly defined through the optimisation framework, which shapes the system output $\Omega(t)$ to track a desired trajectory $\Omega_d(t)$ in response to changes in the reference signal $\Omega_{\text{ref}}(t)$ (or $\Omega_{\text{w}}(t)$ for the tuning stage). Specifically, the optimisation (see Eq. (8)) aims to minimise the tracking error between $\Omega(t)$ and $\Omega_d(t)$ by tuning the controller parameters Θ. The desired trajectory $\Omega_d(t)$ is a 'filtered' version of the reference $\Omega_{\text{w}}(t)$ and reflects a targeted closed-loop response that encodes performance specifications such as settling time or steady-state slope. Two target behaviours are considered in this study: an exponential response and a ramp-like response, defined in Eqs. (41)–(42), which serve as performance benchmarks within the tuning framework.

The role of the tracking error is further emphasised within the control laws: for the PI controller, the error $e(t) = \Omega_{\text{ref}}(t) - \Omega(t)$ is used directly in the feedback; for the SM controller, a sliding variable $\sigma(t) = \Omega_{\text{ref}}(t) - \Omega(t)$, with the corresponding sliding surface given by $\sigma(t) = 0$, is defined to enforce finite-time convergence. Although the desired trajectory $\Omega_d(t)$ is used during the controller tuning stage to encode a specific closed-loop response, the actual control laws operate based on the real-time tracking of the reference $\Omega_{\text{ref}}(t)$ via either $e(t)$ or $\sigma(t)$, depending on the controller. This setup establishes a clear connection between the offline optimisation, the design of the reference trajectory, and the resulting closed-loop dynamics.

For both PI and SM controllers, the task is to tune the parameter vector $\Theta = [k_1, k_2]$ by solving the following optimisation problem:

$$\begin{aligned} \min_{\Theta} \quad & \int_0^T \left(\Omega(t) - \Omega_d(t)\right)^2 dt \\ \text{subject to:} \quad & \dot{x}_c(t) = \mathcal{F}(x_c(t), \Omega_{\text{w}}(t), \Theta), \\ & \Omega(t) = \mathcal{G}(x_c(t)), \\ & \Theta \in \mathcal{P}, \quad u(t) \in \mathcal{U}, \end{aligned} \tag{43}$$

where $x_c(t) = [x^\top(t),\ x_k^\top(t)]^\top$ is the augmented state combining the plant and controller states, and $\mathcal{F}(\cdot)$ represents the closed-loop dynamics obtained by embedding the controller into the plant:

$$\begin{aligned} \dot{x}(t) &= f\left(x(t),\ g_k(x_k(t), e(t), \Theta)\right), \\ \dot{x}_k(t) &= f_k(x_k(t), e(t), \Theta), \\ e(t) &= \Omega_{\text{w}}(t) - g(x(t),\ u(t)), \\ \Omega(t) &= g(x(t),\ u(t)), \end{aligned} \tag{44}$$

as defined in Eqs. (1), (2), and (3). The desired trajectory $\Omega_d(t)$ is defined as a filtered version of $\Omega_{\text{ref}}(t)$, encoding performance specifications such as rise time or convergence slope. This formulation ensures consistency with the fully offline methodology presented in Fig. 1, where the optimiser operates over repeated closed-loop simulations using this closed-loop model. Ultimately, for the application case presented in this section, this study employs MATLAB's Global Optimisation Toolbox (The MathWorks, 2023a), with a focus on pattern search-based routines. Pattern search is selected due to its effectiveness in handling the nonsmooth and constrained nature of the underlying optimisation problem, making it particularly suitable for practical implementation.

4.4. PI control results

4.4.1. Scenario 1

Figs. 4, and 5, present the results of the PI targeting the exponential response, while Fig. 6 presents the results for the PI controller tuned to target the ramp response. Specifically, Fig. 4 shows the effect of varying $\alpha \in \{1, 2, 5, 15\}$, while Fig. 5 explores different values of $\omega \in \{1, 2, 5, 15\}$. In contrast, Fig. 6 illustrates the ramp response case, considering transition durations $t_e \in [0.25, 5, 10, 12]$.

The PI controller shows outstanding performance in the exponential cases (Figs. 4 and 5), achieving near-perfect tracking across all tested values of α and ω. Conversely, for the ramp reference case (Fig. 6), the PI controller exhibits lower performance, showing clear limitations in accurately replicating the ramp family of signals.

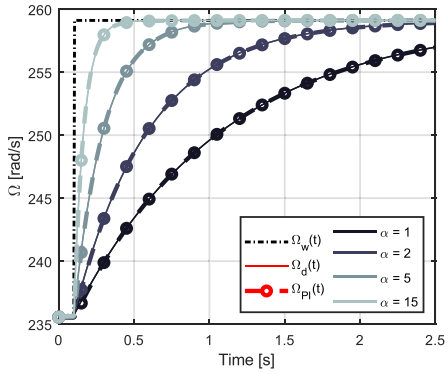

Fig. 4. PI (dashed with circular markers) controller responses with an exponential Ω_d for $\alpha \in [1, 2, 5, 15]$ with $\omega = 0$ (overdamped response). Lighter colours indicate increasing α. Markers highlight sampled points along the trajectories. The red colour in the legend is a neutral reference to indicate the line style. (For interpretation of the references to colour in this figure legend, the reader is referred to the web version of this article.)

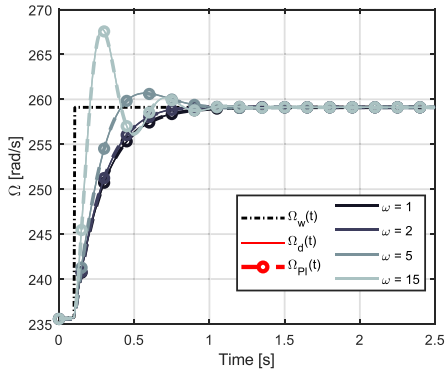

Fig. 5. PI (dashed with circular markers) controller responses with an exponential Ω_d for $\alpha = 5$ with $\omega =\in \{1, 2, 5, 15\}$ (overdamped response). Lighter colours indicate increasing α. Markers highlight sampled points along the trajectories. The red colour in the legend is a neutral reference to indicate the line style. (For interpretation of the references to colour in this figure legend, the reader is referred to the web version of this article.)

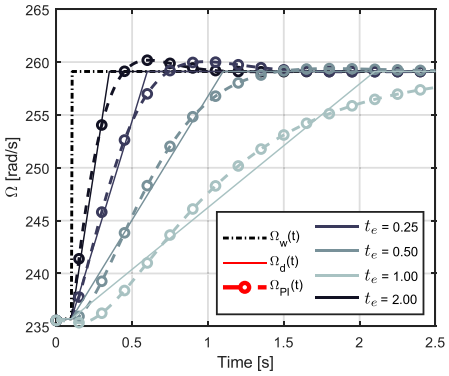

Fig. 6. PI (dashed with circular markers) controller responses with a ramp reference Ω_d for $t_e \in \{0.25, 5, 10, 12\}$. Lighter colours correspond to increasing values of t_e. Markers highlight sampled points along the trajectories. The red colour in the legend is a neutral reference to indicate the line style. (For interpretation of the references to colour in this figure legend, the reader is referred to the web version of this article.)

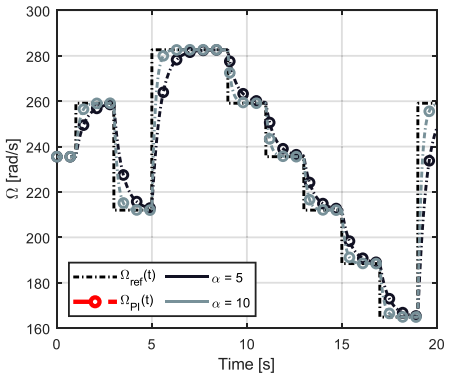

Fig. 7. Stepwise wind profile experiment. PI (dashed with circular markers) controller responses for $\alpha \in \{5, 10\}$ and $\omega = 0$. Lighter colours indicate increasing α. The reference signal $\Omega_{\text{ref}}(t)$ is shown as a black dahs-dotted line. The red colour in the legend is a neutral reference to indicate the line style. (For interpretation of the references to colour in this figure legend, the reader is referred to the web version of this article.)

4.4.2. Scenario 2

The results presented in Fig. 7 demonstrate that the PI controller effectively tracks the stepwise changes in $\Omega_{\text{ref}}(t)$ across the entire dynamic range. The response remains highly consistent with the tuning results in Figs. 4 and 5, exhibiting smooth transitions with no overshoot and convergence to the reference. Increasing α leads to an improvement in tracking speed, reducing the settling time and enhancing accuracy. This behaviour aligns with the expected closed-loop response, confirming the robustness of the PI controller under abrupt variations in the reference signal.

4.4.3. Scenario 3

The results shown in Fig. 8 highlight the performance of the PI controller when tracking a synthetic wind profile. As α increases, the reference tracking speed improves, leading to faster convergence to the reference trajectory $\Omega_{\text{ref}}(t)$. In the zoomed-in section between approximately 33 and 33.5 s, the PI controller demonstrates filtering of the turbulent wind fluctuations. At lower α values, the turbulence is more smoothly filtered out, with minimal tracking of high-frequency components, but also with a degraded performance in the low-frequency components. However, as α increases, the controller begins to replicate the high-frequency fluctuations of the turbulence more closely, indicating a trade-off between tracking accuracy and the degree of closed-loop filtering. This shows that with larger α, the PI controller becomes more responsive to the rapid variations in the synthetic wind profile, potentially improving the tracking of transient behaviours but also introducing more sensitivity to high-frequency fluctuations, which could be undesirable in practical applications.

4.5. Super twisting SMC control results

4.5.1. Scenario 1

Figs. 9 and 10 present the results of the SM controller targeting the exponential response, while Fig. 11 shows the results for the ramp response case. Specifically, Fig. 9 illustrates the effect of varying $\alpha \in \{1, 2, 5, 15\}$ with $\omega = 0$, where the controller achieves a moderate level of performance, albeit with limitations in replicating the overdamped target response. Fig. 10, on the other hand, highlights the considerable challenges in tracking oscillatory references. Among the cases considered, the controller exhibits the best (though still limited) performance for $\omega = 15$, yet it struggles to accurately reproduce the oscillations. In contrast to the PI case, Fig. 11 shows that the SM controller excels in tracking the ramp response, achieving high accuracy across all transition durations $t_e \in \{0.25, 5, 10, 12\}$. The controller exhibits a strong rise, with virtually perfect tracking during the second segment of the target ramp, albeit with a slight overshoot upon reaching the final value Ω_{end}.

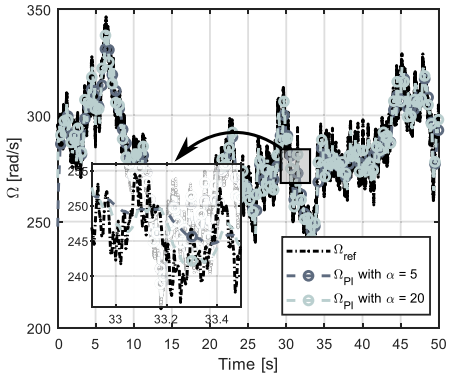

Fig. 8. Realistic wind profile experiment. PI controller (dashed with circular markers) responses for $\alpha \in \{5, 20\}$ and $\omega = 0$. The reference trajectory $\Omega_{\text{ref}}(t)$ is depicted as a black dash-dotted line. A zoomed-in view of the time window between approximately 33 and 33.5 s highlights the tracking performance. Lighter shades represent increasing values of α.

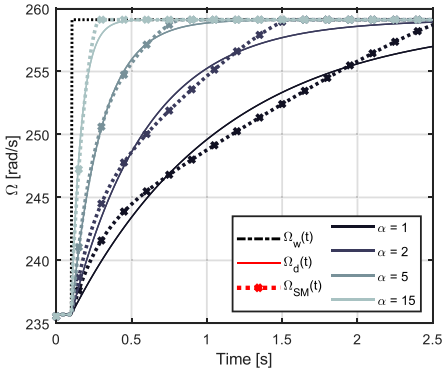

Fig. 9. SM (dotted with cross markers) controller responses with an exponential Ω_d for $\alpha \in \{1, 2, 5, 15\}$ with $\omega = 0$ (overdamped response). Lighter colours indicate increasing α. Markers highlight sampled points along the trajectories. The red colour in the legend is a neutral reference to indicate the line style. (For interpretation of the references to colour in this figure legend, the reader is referred to the web version of this article.)

4.5.2. Scenario 2

The results presented in Fig. 12 show that the SM controller successfully tracks the stepwise changes in $\Omega_{\text{ref}}(t)$, achieving the final value with an overdamped response, as specified in the tuning process. This behaviour is desirable, ensuring smooth convergence without oscillations. However, in contrast to the PI controller, the SM response exhibits noticeable variations depending on the step magnitude and the dynamic range, leading to differences in transient behaviour across the tested conditions. These variations are characteristic of nonlinear systems, where the transient response can significantly depend on the input magnitude and operating conditions. While the controller consistently reaches the reference, these variations highlight its sensitivity to abrupt changes, distinguishing its performance characteristics from the more uniform responses observed with the PI controller. Additionally, increasing α leads to an improvement in tracking speed, reducing the settling time and enhancing accuracy. This behaviour aligns with the expected closed-loop response.

4.5.3. Scenario 3

The results shown in Fig. 13 illustrate the performance of the SM controller when tracking a synthetic wind profile. As with the PI controller, the SM controller improves its tracking speed as α increases, leading to faster convergence to the reference trajectory $\Omega_{\text{ref}}(t)$. At lower α values, the controller demonstrates a smoother filtering of the turbulence, with minimal response to high-frequency fluctuations but also showing degradation in tracking the low-frequency components.

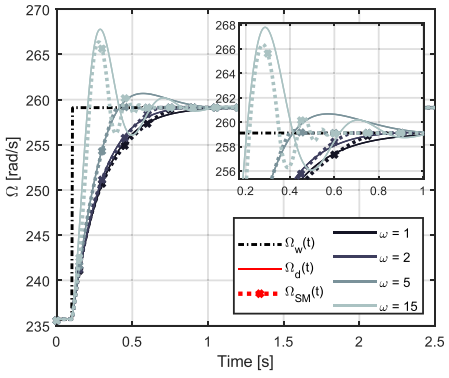

Fig. 10. SM (dotted with cross markers) controller responses with an exponential Ω_d for $\alpha = 5$ with $\omega \in \{1, 2, 5, 15\}$ (damped response). Lighter colours indicate increasing ω. Markers highlight sampled points along the trajectories. The red colour in the legend is a neutral reference to indicate the line style. (For interpretation of the references to colour in this figure legend, the reader is referred to the web version of this article.)

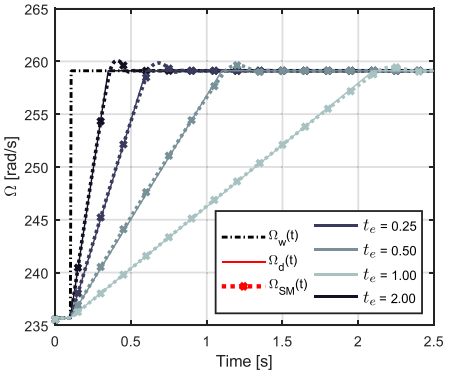

Fig. 11. SM (dotted with cross markers) controller responses with a ramp reference Ω_d for $t_e \in \{0.25, 5, 10, 12\}$. Lighter colours correspond to increasing values of t_e. Markers highlight sampled points along the trajectories. The red colour in the legend is a neutral reference to indicate the line style. (For interpretation of the references to colour in this figure legend, the reader is referred to the web version of this article.)

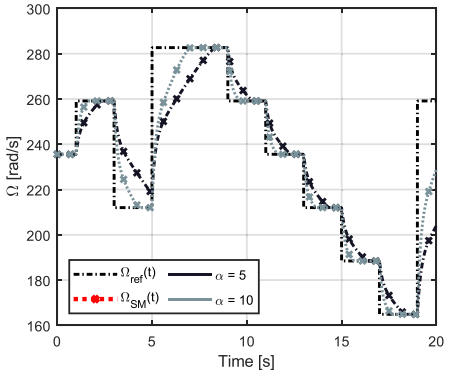

Fig. 12. Stepwise wind profile experiment. PI (dashed with circular markers) and SM (dotted with cross markers) controller responses for $\alpha \in \{5, 10\}$ and $\omega = 0$. Lighter shades indicate increasing α. The reference signal $\Omega_{\text{ref}}(t)$ is shown as a black dotted line. The red colour in the legend is a neutral reference to indicate the line style. (For interpretation of the references to colour in this figure legend, the reader is referred to the web version of this article.)

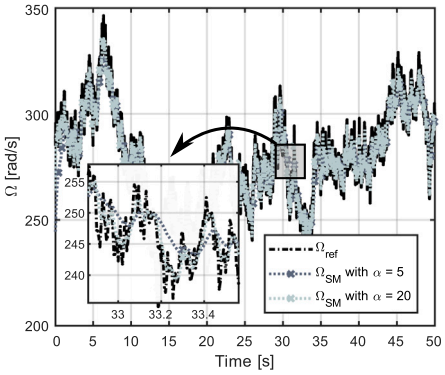

Fig. 13. Realistic wind profile experiment. SM (dotted with cross markers) for $\alpha \in \{5, 20\}$ and $\omega = 0$. The reference trajectory $\Omega_{\text{ref}}(t)$ is shown as a black dash-dotted line. A close-up view of the time span between (approximately) 33 and 33.5 s is shown, highlighting the tracking performance. Lighter shades indicate increasing α values.

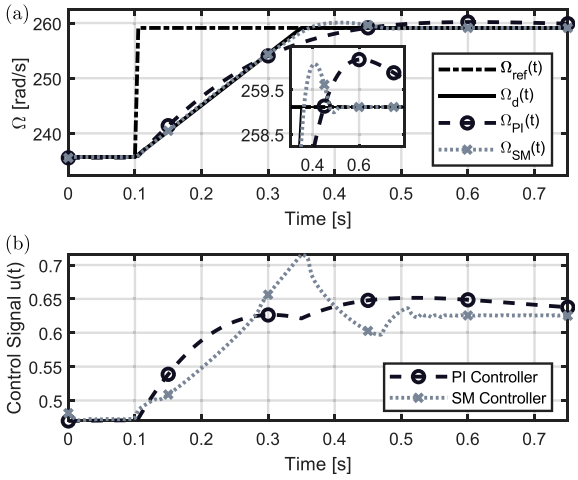

Fig. 14. Ramp case with $t_e = 0.25$. (a) Closed-loop response $\Omega(t)$ for both PI and SM controllers. (b) Control signals for PI and SM controllers, showing consistent magnitude and convergence speed. The control signals are bounded between 0 and 1, which aligns with the actuator's cosine nature. Despite differences in the control signals, both controllers demonstrate similar performance in terms of tracking and response characteristics.

As α increases, the SM controller becomes more responsive to the high-frequency components of the turbulence, closely replicating these rapid variations. This behaviour, while improving transient tracking, introduces a trade-off between tracking accuracy and closed-loop filtering, similar to the PI controller. However, in the fast α case, the SM controller more aggressively replicates the high-frequency components, which, although improving tracking performance in some cases, may still be undesirable in practical applications where excessive sensitivity to high-frequency fluctuations could lead to instability or inefficiency.

5. Discussion

The results presented in Section 4 highlight the effectiveness of the optimisation-based tuning approach in shaping the closed-loop response of nonlinear controllers for wind energy applications. While scenario-specific results and performance trade-offs have been thoroughly analysed in Sections 4.4 and 4.5, the purpose of this section is to provide an integrative discussion that synthesises the main outcomes across all scenarios. One of the most important findings is that different controller configurations, especially for the nonlinear case, can lead to fundamentally distinct closed-loop behaviours. This observation reinforces the need for systematic tuning procedures, since even configurations within theoretically admissible regions (e.g., those satisfying Lyapunov or geometrical conditions Khalil, 1996; Shtessel et al., 2014) may exhibit significantly different convergence and robustness properties. The following discussion reflects on these broader implications and the general performance tendencies observed throughout the study. As shown in Fig. 14, which serves as a representative example from all the analysed cases, the control signals for both the PI and SM controllers, despite some differences, remain consistent in terms of magnitude and convergence speed. Thus, Fig. 14 presents the closed-loop response obtained when applying the proposed tuning approach to both controllers, using a ramp case with $t_e = 0.25$ as the target dynamic. The top plot, Fig. 14(a), illustrates the closed-loop responses $\Omega(t)$ for both controllers, showing how the system tracks the desired trajectory. The bottom plot, Fig. 14(b), displays the corresponding control signals, which remain within the actuator limits, bounded between 0 and 1, in accordance with the cosine actuation nature of the system. Despite the differences in control effort, both controllers exhibit similar tracking performance, reinforcing the effectiveness of the tuning methodology in achieving the prescribed closed-loop behaviour. The results in Fig. 14 illustrate the robustness of the tuning method, ensuring that even with distinct control structures, the overall performance remains aligned with the desired dynamics. The fact that both controllers maintain control signal limits between 0 and 1, which is consistent with the cosine actuation nature of the application case in Section 4, further reinforces the practical viability of the tuning approach, now analysed from the control actuation perspective. This aspect is crucial in real-world applications, where certain closed-loop responses could damage actuator integrity or reduce overall performance.

To further assess the performance of the proposed control strategies under realistic operating conditions, a synthetic wind profile was used to excite the system. This scenario corresponds to the case with $\alpha = 5$ and $\omega = 0$, selected to evaluate the response of both controllers when subjected to realistic disturbances. Fig. 15 presents the resulting closed-loop behaviour. As shown in Fig. 15(a), the SM controller leads to a smoother rotational speed response compared to the PI controller, which exhibits higher-frequency variations due to the turbulent nature of the wind input. This improved tracking comes at the cost of a noisier control signal, as illustrated in Fig. 15(b), where the SM control input displays sharper fluctuations than its PI counterpart. In contrast, the PI controller maintains a smoother control action, highlighting a trade-off between output regularity and control effort smoothness.

The methodology ensures that the closed-loop dynamics adhere to a specific target response, allowing for consistent and effective tuning of the controllers. This is particularly important in nonlinear systems, such as the wind energy case discussed in Section 4, where inherent nonlinearities and external disturbances, such as turbulent wind, pose challenges that cannot be fully addressed by linear approximations or conventional tuning methods.

One of the fundamental advantages of the optimisation-based approach is its ability to offer a structured framework for selecting controller parameters in a way that aligns with the desired system behaviour. This method directly accounts for the inherent nonlinearities, providing a robust solution that goes beyond empirical tuning. Thus, in the application case example in Section 4, the results indicate that tuning parameters, such as α, can significantly impact the transient response, with higher values of α leading to faster convergence to the reference trajectory and a reduction in settling time. However, as shown in Figs. 8 and 13, excessively rapid tracking, particularly in the presence of turbulence, may lead to increased sensitivity to high-frequency components of the wind profile, which could potentially affect mechanical loads and turbine longevity.

Considering the application case, in Fig. 16 the contour plots are presented illustrating the magnitude of the parameter vector Θ =

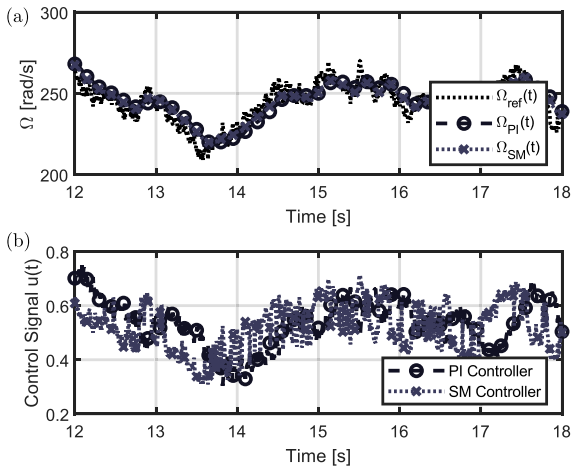

Fig. 15. Closed-loop performance under realistic wind excitation, using the case with $\alpha = 5$ and $\omega = 0$ for control input evaluation. (a) Rotational speed response $\Omega(t)$ for both PI and SM controllers. The SM controller achieves a smoother output response compared to the PI controller, which exhibits higher-frequency variations. (b) Reconstructed control signals show that the PI controller provides a smoother control action, while the SM controller introduces higher-frequency components. This illustrates a trade-off between output smoothness and control effort regularity.

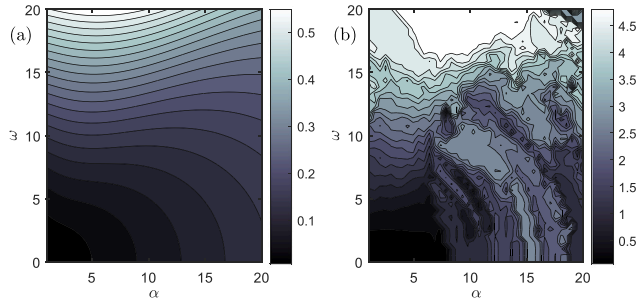

Fig. 16. Contour plots of the magnitude of the parameter vector $\Theta = [K_1, K_2]$ for the PI (a) and SM (b) controllers across the tuning space (α, ω). Darker regions indicate lower sensitivity, while lighter regions correspond to higher sensitivity. The PI plot exhibits smooth variations, suggesting a more stable tuning process, whereas the SM plot reveals regions with sharp transitions, indicating areas of higher sensitivity in the tuning process.

$[K_1, K_2]$, obtained in the exponential target case, across the tuning parameter space (α, ω) for both the PI and SM controllers. The left subplot (a) shows $|\Theta_{PI}|$, while the right subplot (b) depicts $|\Theta_{SM}|$, offering a top-down view, of how the sensitivity of the controller parameters varies with changes in α and ω. Mathematically, the magnitudes are computed as follows:

$$|\Theta_C| = \sqrt{K_1^2 + K_2^2}, \tag{45}$$

where $C \in \{PI, SM\}$ denotes the controller type. Darker regions indicate lower magnitudes, while lighter regions correspond to higher magnitudes of the parameter vector. Abrupt dark-light transitions in the contour plots suggest high sensitivity in the tuning process. In the PI plot, these variations are smooth and gradual, indicating a more stable tuning process. In contrast, the SM plot reveals several areas with sharp transitions, highlighting regions of higher sensitivity. This visualisation emphasises the unintuitive nature of manual or empirical tuning, particularly in nonlinear control, where small changes in one parameter may not correspond to small changes in the controlled system performance. It further underscores the value of the optimisation-based approach as a systematic, automatic methodology that provides a more reliable and consistent process for adjusting controller parameters.

From a wind energy control perspective, the findings highlight the importance of balancing tracking accuracy and robustness in the tuning process. While increasing α enhances tracking precision, the sensitivity to high-frequency turbulence indicates that an intermediate tuning strategy, where α is selected to optimise closed-loop performance without overreacting to wind fluctuations, is more desirable for practical applications.

To quantitatively assess the closed-loop tracking performance of the PI and SM controllers in Scenario 1, considering both exponential and ramp reference targets, four commonly used error metrics are employed to compare the closed-loop response against the desired target trajectory: Mean Absolute Error (MAE), Root Mean Square Error (RMSE), Maximum Absolute Error (MaxErr), and Normalised RMSE (NRMSE). Given a reference trajectory $y_d(t)$ and a closed-loop response $y(t)$, these metrics are formally defined as follows:

$$\begin{aligned}
\text{MAE} &= \frac{1}{N}\sum_{i=1}^{N} \left|y_d(t_i) - y(t_i)\right|, \\
\text{RMSE} &= \sqrt{\frac{1}{N}\sum_{i=1}^{N} \left(y_d(t_i) - y(t_i)\right)^2}, \\
\text{MaxErr} &= \max_{1\le i\le N} \left|y_d(t_i) - y(t_i)\right|, \\
\text{NRMSE} &= \frac{\text{RMSE}}{\max(y_d) - \min(y_d)}.
\end{aligned} \tag{46}$$

These metrics assess the overall magnitude of the performance error (MAE), penalise larger deviations (RMSE), highlight worst-case errors (MaxErr), and offer a normalised performance measure (NRMSE) that accounts for the range of the reference signal. Additionally, a performance ratio is computed as the quotient of each metric for the PI controller divided by that of the SM controller. A ratio greater than 1 indicates better performance of the SM controller, while a ratio less than 1 suggests the PI controller achieves more accurate tracking.

As summarised in Table 2, the error metrics reveal a distinct difference in closed-loop capabilities between the two controllers, depending on the target dynamics. Without the intention of performing a direct comparative analysis, the third row in each case (Ratio PI/SM) is included solely to emphasise the importance of defining a suitable closed-loop dynamic that aligns with the capabilities and characteristics of each control strategy. For exponential target profiles, which are characterised by parameters α and ω, defined in Eq. (41) and shown in the top part of the table, the PI controller generally outperforms the SM controller across all error metrics. In these cases, the PI/SM ratios remain consistently below 1, with values ranging from approximately 0.04 to 0.27 depending on the metric, confirming the superior ability of the PI controller to track exponential transients more closely.

Conversely, for ramp target profiles, specified by the settling time parameter t_c, defined in Eq. (42) and shown in the bottom portion of the table, the SM controller consistently outperforms the PI controller. Here, the error metric ratios are significantly greater than 1, often exceeding values of 5 or 17 in the case of NRMSE. This highlights the robustness and effectiveness of the SM controller in accurately reproducing the linear rise of the ramp reference, regardless of the steepness of the transition (i.e., $t_s = 0.25, 0.5, 1.0, 2.0$ seconds).

Overall, this analysis illustrates the complementary strengths of the two controller types under different reference trajectories: the PI controller excels at following smooth, exponentially converging profiles, while the SM controller is more suitable for aggressive, ramp-like transients. These findings support the necessity of custom tuning strategies based on the desired system dynamics and reinforce the flexibility of the optimisation-based framework presented in this work.

To further illustrate how the controller gains are shaped by the desired closed-loop dynamics, Fig. 17 presents the tuned parameters k_1 and k_2 for both PI and SM controllers across the design space explored

Table 2
Comparison of error metrics (MAE, RMSE, MaxErr, and NRMSE) for PI and SM controllers in Scenario 1 under exponential and ramp reference targets. Ratio rows express the quotient PI/SM for each metric.

Scenario 1 – Error Metrics (Exponential Targets)							
α	ω	t_s [s]	Controller	MAE [rad/s]	RMSE [rad/s]	MaxErr [rad/s]	NRMSE
1	0	–	PI	0.0319	0.0550	0.2295	0.0026
1	0	–	SM	0.7881	0.9151	1.7108	0.0430
1	0	–	Ratio PI/SM	0.0405	0.0601	0.1342	0.0601
2	0	–	PI	0.0308	0.0549	0.2709	0.0024
2	0	–	SM	0.6012	0.6968	1.3132	0.0300
2	0	–	Ratio PI/SM	0.0513	0.0787	0.2063	0.0787
5	0	–	PI	0.0264	0.0560	0.3981	0.0024
5	0	–	SM	0.1257	0.2061	0.6298	0.0088
5	0	–	Ratio PI/SM	0.2103	0.2719	0.6321	0.2719
15	0	–	PI	0.0238	0.0710	0.8401	0.0030
15	0	–	SM	0.0914	0.2844	1.5274	0.0122
15	0	–	Ratio PI/SM	0.2601	0.2495	0.5500	0.2495
5	2	–	PI	0.0261	0.0553	0.3952	0.0024
5	2	–	SM	0.0806	0.1445	0.5313	0.0062
5	2	–	Ratio PI/SM	0.3245	0.3826	0.7438	0.3826
5	5	–	PI	0.0233	0.0538	0.3864	0.0022
5	5	–	SM	0.2308	0.4896	1.5678	0.0196
5	5	–	Ratio PI/SM	0.1009	0.1100	0.2464	0.1100
5	15	–	PI	0.0368	0.0741	0.3604	0.0023
5	15	–	SM	0.6295	1.3837	5.8657	0.0431
5	15	–	Ratio PI/SM	0.0584	0.0535	0.0614	0.0535
Scenario 1 – Error Metrics (Ramp Targets)							
α	ω	t_s [s]	Controller	MAE [rad/s]	RMSE [rad/s]	MaxErr [rad/s]	NRMSE
–	–	0.25	PI	0.3051	0.5778	2.6929	0.0247
–	–	0.25	SM	0.0495	0.1687	0.9685	0.0072
–	–	0.25	Ratio PI/SM	6.1621	3.4242	2.7804	3.4242
–	–	0.50	PI	0.3686	0.5520	2.1167	0.0236
–	–	0.50	SM	0.0610	0.1578	0.7413	0.0067
–	–	0.50	Ratio PI/SM	6.0425	3.4986	2.8553	3.4986
–	–	1.00	PI	0.5107	0.6761	1.8487	0.0289
–	–	1.00	SM	0.0906	0.1514	0.5186	0.0065
–	–	1.00	Ratio PI/SM	5.6375	4.4668	3.5651	4.4668
–	–	2.00	PI	1.2242	1.3899	2.6393	0.0584
–	–	2.00	SM	0.0703	0.1098	0.3430	0.0047
–	–	2.00	Ratio PI/SM	17.4120	12.6562	7.6952	12.6562

in Scenario 1. The plots show how the controller gains vary with respect to the real part α, the imaginary part ω, and the desired rise time t_e, revealing clear trends and differences between the two control structures. These results complement the contour maps in Fig. 16 by providing an explicit gain-level view of the tuning landscape, reinforcing the importance of systematic offline optimisation in defining meaningful and physically consistent parameter sets.

6. Conclusion

This study demonstrates the effectiveness, versatility, and robustness of the presented optimisation-based tuning procedure for nonlinear controllers, particularly in the context of complex nonlinear systems. The primary strength of the method lies in its ability to systematically identify controller parameters that shape the closed-loop dynamics according to specific, pre-defined targets. This provides a practical and structured alternative to the traditional trial-and-error tuning strategies commonly employed by practitioners for control tuning. In addition to its simplicity and adaptability across a wide range of applications, a key contribution of this work is the definition of a framework that makes explicit the concept of reachable closed-loop dynamics in nonlinear systems, analogous to the classical behaviours typically observed in linear control systems, such as exponential convergence, damped oscillations, or ramp-like responses. By enabling these target behaviours to be systematically achieved through informed tuning, the methodology can ensure not only precise dynamic shaping but also robustness and stability under varying operating conditions. The results underscore the sensitivity of nonlinear controllers to tuning parameters, revealing that different configurations can lead to significantly different closed-loop behaviours, even within theoretically admissible ranges. This parameter-dependent behaviour highlights the inherent complexity of nonlinear control tuning and reinforces the importance of selecting parameters that ensure both performance and system longevity. The scope of the proposed method is general and independent of the specific structure of the nonlinear controller or the application domain. The novelty lies in explicitly linking tuning with the desired closed-loop dynamics, using a performance-driven optimisation framework that is both interpretable and adaptable.

The optimisation-based approach provides a structured and reliable framework to achieve a precise closed-loop dynamic response, addressing the nonlinear nature of the system. By accounting for these nonlinearities, the method allows for the customisation of controller parameters that optimise system performance, ensuring that the system adheres to the desired target response across a range of operational scenarios. Importantly, this approach offers a robust solution that goes beyond traditional empirical tuning, delivering consistent and effective controller performance while preventing actuator overloading and maintaining system longevity.

In conclusion, the study highlights the importance of carefully selecting controller parameters, as small changes can result in significant variations in the closed-loop dynamics. The optimisation-based procedure not only ensures precise control but also enhances the overall robustness, which is validated in this study in a wind energy example, providing a reliable and adaptive solution for complex, nonlinear control problems.

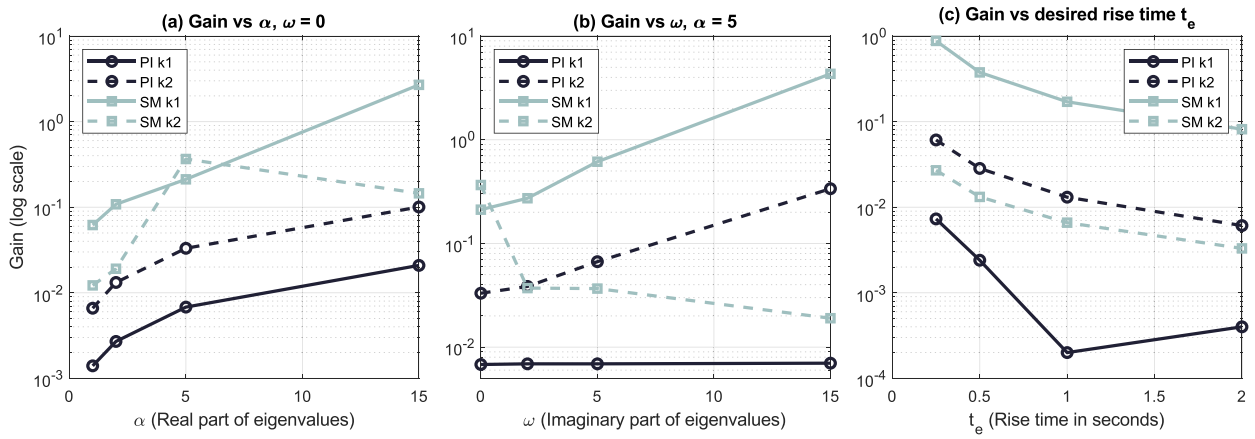

Fig. 17. PI and SM controller gains (k_1, k_2) tuned for Scenario 1. (a) Gains vs real part α with $\omega = 0$. (b) Gains vs imaginary part ω at $\alpha = 5$. (c) Gains vs desired rise time t_e. Colours differentiate PI (blue) and SM (red) controllers, illustrating gain variation with target closed-loop dynamics. (For interpretation of the references to colour in this figure legend, the reader is referred to the web version of this article.)

CRediT authorship contribution statement

Demián García-Violini: Writing – review & editing, Writing – original draft, Visualization, Validation, Supervision, Software, Resources, Project administration, Methodology, Investigation, Funding acquisition, Formal analysis, Data curation, Conceptualization. **Carolina A. Evangelista:** Writing – review & editing, Validation, Supervision, Project administration, Methodology, Investigation, Formal analysis, Conceptualization. **Yerai Peña-Sanchez:** Writing – review & editing, Validation, Software, Investigation, Conceptualization. **Paul Puleston:** Writing – review & editing, Supervision, Project administration, Formal analysis, Conceptualization.

Declaration of competing interest

The authors declare that they have no known competing financial interests or personal relationships that could have appeared to influence the work reported in this paper.

Acknowledgements

Demián García-Violini is supported by the Fondo Argentino Sectorial (FONARSEC) through the Agencia I+D+i, under project PE TRA N° 08 (RESOL 2022-290 APNDANPIDTYI#). Additionally, Demián García-Violini receives financial support from Agencia I+D+i via the PICT-2021-I-INVI-00190 grant. Yerai Peña-Sanchez is funded by MCIN/AEI/10.13039/50 1100011033 and by ERDF: A way of making Europe under the *HYBRID* research project (PID2021-124245OA-I00), and by the Basque Government's ELKARTEK 2024 program under the *RUL-ET* research project (KK-2024/00086).

References

Baroudi, J. A., Dinavahi, V., & Knight, A. M. (2007). A review of power converter topologies for wind generators. *Renewable Energy*, *32*(14), 2369–2385.

Baroudi, J., Dinavahi, V., & Knight, A. (2007). A review of power converter topologies for wind generators. *Renewable Energy*, *32*(14), 2369–2385.

Bendjeddou, Y., Deboucha, A., Bentouhami, L., Merabet, E., & Abdessemed, R. (2021). Super twisting sliding mode approach applied to voltage orientated control of a stand-alone induction generator. *Protection and Control of Modern Power Systems*, *6*(2), 1–9.

Bianchi, F. D., de Battista, H., & Mantz, R. (2007). *Wind turbine control systems: Principles, modeling and gain scheduling design*. Springer.

Boersma, S., Doekemeijer, B. M., Gebraad, P. M., Fleming, P. A., Annoni, J., Scholbrock, A. K., Frederik, J. A., & van Wingerden, J. W. (2017). A tutorial on control-oriented modeling and control of wind farms. In *2017 American control conference* (pp. 1–18). IEEE.

Bose, B. (2002). Modern power electronics and AC drives. In *Eastern economy edition*, Prentice Hall PTR.

Bujgoi, G., & Sendrescu, D. (2024). Tuning of PID controllers using reinforcement learning for nonlinear systems control.

Burton, T., Jenkins, N., Sharpe, D., & Bossanyi, E. (2011). *Wind energy handbook*. John Wiley & Sons, Ltd, http://dx.doi.org/10.1002/9781119992714.

Cadirci, I., & Ermis, M. (1992). Double-output induction generator operating at subsynchronous and supersynchronous speeds: Steady-state performance optimisation and wind energy recovery. *IEE Proceedings-B Electric Power Applications*, *139*(5), 429–442, URL: https://hdl.handle.net/11511/64925.

Charkoutsis, S., & Kara-Mohamed, M. (2023). A particle swarm optimization tuned nonlinear PID controller with improved performance and robustness for first order plus time delay systems. *Results in Control and Optimization*, *12*, Article 100289.

De Battista, H., Mantz, R. J., & Christiansen, C. F. (2001). Performance analysis of a variable structure controller for power regulation of WECS operating in the stall region. *International Journal of Energy Research*, *25*(15), 1345–1357. http://dx.doi.org/10.1002/er.758.

Dekali, Z., Baghli, L., & Boumediene, A. (2021). Improved super twisting based high order direct power sliding mode control of a connected DFIG variable speed wind turbine. *Periodica Polytechnica Electrical Engineering and Computer Science*, *65*(4), 352–372.

Evangelista, C., Puleston, P., & Valenciaga, F. (2010). Wind turbine efficiency optimization. Comparative study of controllers based on second order sliding modes. *International Journal of Hydrogen Energy*, *35*(11), 5934–5939.

Evangelista, C., Puleston, P., Valenciaga, F., & Dávila, A. (2010). Variable gains super-twisting control for wind energy conversion optimization. In *11th int. workshop on variable structure systems* (pp. 50–55). México D.F., México: http://dx.doi.org/10.1109/VSS.2010.5544713.

Evangelista, C., Puleston, P., Valenciaga, F., & Fridman, L. M. (2013). Lyapunov-designed super-twisting sliding mode control for wind energy conversion optimization. *IEEE Transactions on Industrial Electronics*, *60*(2), 538–545. http://dx.doi.org/10.1109/TIE.2012.2188256.

Fridman, L., Moreno, J. A., Bandyopadhyay, B., Kamal, S., & Chalanga, A. (2015). Continuous nested algorithms: The fifth generation of sliding mode controllers. In X. Yu, & M. Önder Efe (Eds.), *Recent advances in sliding modes: from control to intelligent mechatronics* (pp. 5–35). Springer International Publishing.

Goodwin, G. C., Graebe, S. F., Salgado, M. E., et al. (2001). *Control system design: vol. 240*, Prentice Hall New Jersey.

Guozden, T. M., Bianchi, E., Solarte, A., & Mulleady, C. (2018). Wind resource assessment in the rio negro province (Patagonia Argentina) using MERRA reanalysis. *Meteorologica*, *43*(2), 47–61.

Haiqing, Y., Panda, S. K., & Chii, L. Y. (1996). Performance comparison of sliding mode control with PI control for four-quadrant operation of switched reluctance motors. In *Proceedings of international conference on power electronics, drives and energy systems for industrial growth: vol. 1*, (pp. 381–387). IEEE.

Hiskens, I. A. (2002). Systematic tuning of nonlinear power system controllers. In *Proceedings of the international conference on control applications: vol. 1*, (pp. 19–24). IEEE.

International Electrotechnical Commission (2019). *(IEC 61400-1) Wind turbines – Part 1: Design requirements* (4th ed.). (61400–1), Geneva, Switzerland: IEC, International Electrotechnical Commission, URL: https://webstore.iec.ch/en/publication/26423. Edition 4.0.

Kaimal, J., & Finnigan, J. (1985). Spectral characteristics of surface layer turbulence. *Boundary-Layer Meteorology*, *33*(1), 15–34.

Kaimal, J. C., Wyngaard, J. C., Izumi, Y., & Coté, O. R. (1972). Spectral characteristics of surface-layer turbulence. *Quarterly Journal of the Royal Meteorological Society*, *98*(417), 563–589.

Khalil, H. K. (1996). *Noninear systems*. New Jersey: Prentice-Hall.

Labriola, C. (2020). Wind energy in Argentina: Actuality and prospects. In *The age of wind energy: Progress and future directions from a global perspective* (pp. 147–173). Springer.

Locatelli, M., & Schoen, F. (2013). *Global optimization: Theory, algorithms, and applications*. SIAM.

Mayosky, M., & Cancelo, I. (1999). Direct adaptive control of wind energy conversion systems using Gaussian networks. *IEEE Transactions on Neural Networks*, *10*(4), 898–906. http://dx.doi.org/10.1109/72.774245.

Mpanza, L. J., & Pedro, J. O. (2021). Optimised tuning of a PID-based flight controller for a medium-scale rotorcraft. *Algorithms*, *14*(6), 178.

Munteanu, I., Bratcu, A., Cutululis, N., & Ceanga, E. (2008). *Optimal control of wind energy systems*. Springer-Verlag London.

Papageorgiou, D. (2022). Towards prescribed accuracy in under-tuned super-twisting sliding mode control loops - experimental verification. In *2022 American control conference* (pp. 2503–2508). http://dx.doi.org/10.23919/ACC53348.2022.9867161.

Papageorgiou, D., & Edwards, C. (2021). On the behaviour of under-tuned super-twisting sliding mode control loops. arXiv. Stability and performance under periodic perturbations.

Pazmiño, R., Pavon, W., Armstrong, M., & Simani, S. (2024). Performance evaluation of fractional proportional–integral–derivative controllers tuned by heuristic algorithms for nonlinear interconnected tanks. *Algorithms*, *17*(7), 306.

Peña-Sanchez, Y., Centeno-Telleria, M., Zarketa-Astigarraga, A., Penalba, M., García-Violini, D., Faedo, N., & Ringwood, J. (2024). Efficient wave energy converter optimisation via control co-design: A comparison of AI-based algorithms. In *Innovations in renewable energies offshore* (pp. 535–542). CRC Press.

Petronijević, M., Peruničić-Draženović, B., Milosavljavić, v., & Veselić, B. (2017). Discrete-time speed servo system design–a comparative study: Proportional–integral versus integral sliding mode control. *IET Control Theory & Applications*, *11*(16), 2671–2679.

Puleston, P. F., Mantz, R. J., Battaiotto, P. E., & Valenciaga, F. (2000). Sliding mode control for efficiency optimization of wind energy systems with double output induction generator. *International Journal of Energy Research*, *24*(1), 77–92.

Rosendo, J. L., Monnet, D., De Battista, H., Ninin, J., Clement, B., & Garelli, F. (2021). A global optimization approach for sliding mode tuning and existence maps generation. *International Journal of Dynamics and Control*, *9*, 658–670.

Rubio, L., Ibeas, A., & Luo, X. (2016). P-PI and super twisting sliding mode control schemes comparison for high-precision CNC machining. In *2016 24th Iranian conference on electrical engineering* (pp. 1825–1830). IEEE.

SciPy Community (2023). Scipy: Scientific library for python. URL: https://scipy.org/. (Accessed 10 February 2023).

Sehab, R., Akrad, A., & Saadi, Y. (2023). Super-twisting sliding mode control to improve performances and robustness of a switched reluctance machine for an electric vehicle drivetrain application. *Energies*, *16*(7), 3212.

Shtessel, Y., Edwards, C., Fridman, L., & Levant, A. (2014). *Sliding mode control and observation*. Springer New York, http://dx.doi.org/10.1007/978-0-8176-4893-0.

Slotine, J. J. E., Li, W., et al. (1991). *Applied nonlinear control*: *vol. 199*, (1), Prentice hall Englewood Cliffs, NJ.

Spée, R., Bhowmik, S., & Enslin, J. H. (1995). Novel control strategies for variable-speed doubly fed wind power generation systems. *Renewable Energy*, *6*(8), 907–915.

Stull, R. B. (2012). *An introduction to boundary layer meteorology*: *vol. 13*, Springer Science & Business Media.

The MathWorks, I. (2023). Global Optimization Toolbox. URL: https://www.mathworks.com/products/global-optimization.html. (Accessed 10 February 2023).

The MathWorks, I. (2023). Ordinary Differential Equation Solvers. URL: https://www.mathworks.com/help/matlab/ordinary-differential-equations.html. (Accessed 10 February 2023).

Utkin, V. I. (1992). *Sliding modes in control and optimization*. Berlin, Germany: Springer-Verlag.

Zambrano-Gutierrez, D. F., Cruz-Duarte, J. M., Castañeda, H., & Avina-Cervantes, J. G. (2024). Optimization of adaptive sliding mode controllers using customized metaheuristics in DC-DC buck-boost converters. *Mathematics*, *12*(23), 3709.